Vignetting Correction Using an Optical Model and Constant Chromaticity Prior

Beinan Yu, Jiacheng Ying, Lun Luo, *Member, IEEE*, Si-Yuan Cao, Xiansong Bao, and Hui-Liang Shen, *Member, IEEE*

***Abstract*—Vignetting correction is a key pre-processing module for most imaging systems related to computer vision applications. Vignetting estimation is difficult for the current imaging systems due to the complex optical components and challenging vignetting feature extraction. In this work, we propose an algorithm for single-image vignetting correction. We present an optical aperture limit model that uses an occlusion parameter to estimate vignetting effect caused by light occlusion. Moreover, we derive a novel prior that the pixel chromaticity is not affected by vignetting. Our algorithm efficiently selects regions for feature extraction according to the chromatic and spatial analysis of the image, and then uses the intensity ratios to predict the vignetting model parameters and optical center guided by the constant chromaticity prior. We evaluate our algorithm on both synthetic and real-world images. Experimental results indicate that, compared with the state-of-the-art methods, our algorithm achieves better correction under different types of vignetting.**

***Index Terms*—Vignetting correction, aperture limit model, constant chromaticity prior, light occlusion, optical model.**

I. Introduction

VIGNETTING is a common but undesirable effect in an image due to the intrinsic drawbacks of imaging systems. It refers to the radial attenuation of brightness away from the image center. Vignetting has a negative impact on the performance of the computer vision tasks that are sensitive to the intensity of pixels, such as stereo matching [1], object detection [2], image mosaicing [3], and image segmentation [4]. Therefore, vignetting correction is an essential pre-processing step for current imaging systems to obtain high-quality images.

Manuscript received 16 January 2023; revised 9 May 2023 and 17 September 2023; accepted 4 November 2023. Date of publication 17 November 2023; date of current version 22 November 2023. This work was supported in part by the "Pioneer" and "Leading Goose" R&D Program of Zhejiang under Grant 2023C03136 and in part by the Zhejiang Provincial High-level Talents Special Support Program under Grant 2020R52003. The associate editor coordinating the review of this manuscript and approving it for publication was Dr. Mauricio Delbracio. *(Corresponding authors: Si-Yuan Cao; Hui-Liang Shen.)*

Beinan Yu, Jiacheng Ying, Lun Luo, and Hui-Liang Shen are with the College of Information Science and Electronic Engineering, Zhejiang University, Hangzhou 310027, China (e-mail: mr_vernon@hotmail.com; yingjiacheng@zju.edu.cn; luolun@zju.edu.cn; shenhl@zju.edu.cn).

Si-Yuan Cao is with the Ningbo Research Institute, Zhejiang University, Ningbo 315100, China, and also with the College of Information Science and Electronic Engineering, Zhejiang University, Hangzhou 310027, China (e-mail: karlcao@hotmail.com).

Xiansong Bao is with the Anhui NARI Jiyuan Electric Power System Tech Company Ltd., Hefei 230000, China (e-mail: baoxiansong@sgepri.sgcc.com.cn).

Source code is available at http://ivlab.org/publications.html.

Digital Object Identifier 10.1109/TCI.2023.3332229

Several factors can lead to different types of vignetting. Natural vignetting is caused by off-axis illumination falloff that follows the $\cos^4$ law [5], [6]. Pixel vignetting arises from the variation in light striking angles of different pixels in a sensor. Optical vignetting occurs when the lens components block the incident light and is more significant with wide-angle lenses. Mechanical vignetting emerges with occlusion by those unsupported imaging components entering the field of view. Some optical models [5], [6], [7], [8], [9] have been introduced to model vignetting in the imaging process. Kang-Weiss (KW) [8] model uses off-axis illumination factor, geometric factor, and tilt factor to construct a vignetting function, and the extended KW model [9] improves the geometric and tilt factors. These models provide a close fit to the observed vignetting effect except for the mechanical vignetting. However, there are few models for vignetting caused by small apertures, though this type of vignetting is common in multispectral imaging systems [10], [11], microscopes [12], and etc. In these systems, the apertures of optical components and imaging devices can be unmatched since they are made by different manufacturers. As the customization of optical components are difficult and costly, vignetting effect is unavoidable and should be corrected for relevant downstream vision tasks.

Various computational techniques have been presented to correct vignetting effect during the imaging process. The calibration-based methods [7], [8], [13] obtain a template image from a uniform object and measure the corresponding intensity response at each pixel to correct vignetting. Multiple-image-based methods [14], [15], [16], [17] capture image sequences and solve the vignetting function using the information from multiple images. These methods remove vignetting effectively but require either a calibration image or image sequences to derive vignetting features. On the other hand, single-image-based methods [9], [18], [19], [20], [21], [22] restore vignetting-free images without additional information. These methods extract the characteristics of vignetting in a single image and produce results of high quality in an automatic manner. However, the existing single-image-based methods still face some challenges such as heavy computations, optical center prediction, and distinguishing the brightness attenuation of vignetting and scene textures.

In this work, we propose an algorithm to correct vignetting effect using a single image. Based on a typical optical imaging model, we propose an aperture limit model to precisely describe the brightness attenuation caused by light occlusion. This model integrates the intrinsic optical parameters of the imaging system into a single occlusion parameter. With this parameter, we can precisely model the brightness fall-off caused by light occlusion and improve the efficiency of parameter estimation. Moreover, we introduce a novel constant chromaticity prior for vignetting correction that the chromaticity of a pixel is not affected by vignetting though its intensity decreases. We develop an effective vignetting correction algorithm that consists of two main modules for vignetting estimation. First, we analyze the chromatic and spatial information of the image and select these local regions for feature extraction. Guided by the constant chromaticity prior, we then exploit the intra-region intensity ratios of different selected regions to estimate vignetting. Distinct from the previous methods, our algorithm considers the challenges of vignetting estimation comprehensively and predicts both the model parameters and the optical center from the potential vignetting regions. Experimental results demonstrate that our algorithm outperforms previous approaches for single-image-based vignetting correction. In summary, the main contributions of this work are as follows.

- We present an aperture limit optical model for the precise description of the vignetting effect caused by light occlusion.
- We propose an effective vignetting correction algorithm that effectively estimates vignetting function and optical center guided by a novel constant chromaticity prior.
- Our experiments validate that the proposed algorithm is also applicable to removing other types of vignetting and outperforms the state-of-the-art correction methods.

The rest of this article is organized as follows. Section II reviews the previous work related to vignetting model and correction methods. Section III introduces the proposed optical model of mechanical vignetting. Section IV elaborates the implementation details of the correction algorithm. Section V shows the experimental results. Finally, Section VI concludes this work.

II. Related Work

In this section, we briefly review the previous work related to vignetting models and vignetting correction methods.

A. Vignetting Models

Several vignetting models have been introduced for vignetting estimation. Since the vignetting effect is radial in nature, most methods analyze vignetting in polar coordinates and use $V(r)$ to denote the attenuation proportion at the distance of r. We coarsely categorize the previous models into two types, i.e., empirical models [14], [23], [24] and physical models [5], [6], [7], [8], [9].

The empirical models use typical functions to describe the radial intensity attenuation. Based on the observation of the reference images with vignetting, a 6th-order even polynomial function is employed to approximate the vignetting effect [14],

$$V_{\text{Polynomial}}(r) = 1 + \alpha_2 r^2 + \alpha_4 r^4 + \alpha_6 r^6, \tag{1}$$

where α_2, α_4, and α_6 are the polynomial coefficients. This polynomial function produces a close fit to natural and optical vignetting, and performs well on camera calibration.

Some vignetting correction methods exploit hyperbolic functions to model vignetting. The two-dimensional (2-D) hypercosine model [24] considers the brightness falloff of vertical and horizontal directions,

$$V_{\text{Hypercos}}(r,\theta) = \frac{1}{\cosh(c_x r\cos\theta)\cosh(c_y r\sin\theta) + c}, \tag{2}$$

where (r,θ) is the polar coordinate of the corresponding pixel, c_x and c_y denote falloff rates along the x and y dimensions of the image, and c denotes a constant bias. The 2-D hypercosine model is applicable for those embedded digital imaging systems with limited memory resources.

The physical models estimate the vignetting effect according to the optical analysis of the imaging process. Driven by the optics measured known beforehand, the physical models may be more reasonable than these empirical models. Several physical models have been introduced based on different optical factors. The off-axis illumination model [5], [6] is derived from a simple model consisting of a thin lens and an imaging plane, formulated as

$$V_{\text{Off-Axis}}(r) = \frac{1}{(1+(r/f)^2)^2}, \tag{3}$$

where f denotes the focal length of the lens. The off-axis illumination model accounts for vignetting caused by a single lens, yet it is not generic for the imaging systems with multiple lenses.

The variable cone (VC) model [7] considers the additional factor of light occlusion by a set of lenses,

$$V_{\text{VC}}(r) = \frac{c_n S_{\text{out}}(r)}{(1+(r/f)^2)^2}, \tag{4}$$

where $S_{\text{out}}(r)$ is the exit pupil and c_n is the normalization coefficient. The variable cone model successfully predicts vignetting distortion but suffers from the severe constraints of the imaging system parameters such as light axis and field of view.

The Kang-Weiss (KW) model [8] additionally considers the camera tilt effect in the imaging procedure. This model incorporates the off-axis illumination, light obstruction, and tilt effects to formulate vignetting as

$$V_{\text{KW}}(r) = \frac{G(r)T(r)}{(1+(r/f)^2)^2}, \tag{5}$$

where the geometric factor $G(r) \approx 1 - \alpha r$ denotes the approximation of light obstruction, and the tilt factor $T(r)$ denotes the image tilt function. The KW model is reliable for those common digital cameras, and is widely employed in various existing vignetting correction algorithms.

The extended KW model [9] improves the geometric and tilt factors, and maintains the same form as the Kang-Weiss model

$$V_{\text{Extended-KW}}(r) = \frac{G_e(r)T_e(r)}{(1+(r/f)^2)^2}, \tag{6}$$

where the geometric factor $G_e(r) = 1 - \sum_{i=1}^{p} \alpha_i r^i$ is generalized to a polynomial form, and the tilt factor $T_e(r)$ is a region-aware function for which different image regions have different tilt angles. These improvements make the model applicable to more complex scenes.

We note that these existing models are designed to estimate vignetting in images captured by typical imaging systems. However, as the current imaging systems become more and more sophisticated, these models may not provide a precise description of vignetting. Instead, our aperture limit model mainly considers the incident light obstruction factor of vignetting. Our model analyzes the optical structure of imaging systems with small apertures and uses an occlusion parameter to model vignetting effect.

B. Vignetting Correction

Different techniques have been introduced to estimate vignetting in the imaging process and restore vignetting-free images. We can classify the popular vignetting correction methods into calibration-based, multiple-image-based, and single-image-based approaches.

The calibration-based approaches [7], [8], [13] estimate vignetting by obtaining a template image under uniform illumination. For example, the VC model [7] utilizes a white acrylic filter to capture reference images for vignetting correction. The KW model [8] solves vignetting parameters using an image of Lambertian surface. The 2-D harmonic Gaussian filter [13] extracts the vignetting features from the image of an integrating sphere. With the assistance of a reference image, the calibration-based approaches accurately estimate the attenuation proportion and achieve satisfactory vignetting calibration. However, they are barely suitable for the current complex imaging system with tunable optical components since the uniform reference is unavailable in practice.

The multiple-image-based approaches [14], [15], [16], [17] analyze vignetting characteristics based on the assumption that the vignetting function is identical for image sequence. Some methods [15], [16] estimate vignetting through the scene information in a moving image sequence. They select overlapping views in the image sequence for vignetting removal, and produce effective restored results. Other methods [14], [17] compute vignetting parameters from images acquired with different camera settings such as aperture and exposure time, and generate the vignetting function to recover the vignetting-free images. However, these approaches are time-consuming and constrained by real-time tasks.

Single-image-based approaches [9], [12], [18], [19], [20], [21], [22] correct vignetting for an arbitrary image. Considering that vignetting is a low-frequency degradation in an image, some algorithms [9], [18] decompose an image into several homogeneous regions according to texture information, and then estimate vignetting based on low-frequency brightness variation within each region. These methods effectively correct vignetting but they rely on accurate image segmentation and ignore the problem of optical center location. Some other algorithms estimate vignetting under the guidance of some priors derived from image statistics. For example, based on the observation that the gradient distribution symmetries (GDS) are

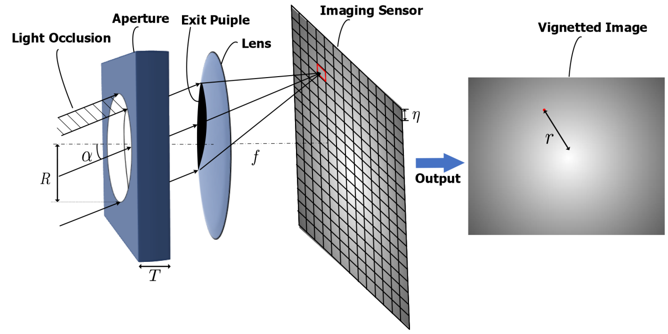

Fig. 1. Our aperture limit optical model that consists of an aperture, a lens, and an imaging sensor. During the imaging process, the aperture blocks part of the light and causes pixel intensity attenuation. The proportion of occlusion gradually increases with the enlargement of the incident angle α, which means that the intensity of the pixel farther from the optical center falls off more severely.

closely related to vignetting in images, the work [19] predicts vignetting function by minimizing the asymmetries of gradient distributions. Based on the radial bright channel (RBC) prior that the maximal pixel intensity at each radius is almost the same for those vignetting-free images, the work [20] computes a one-dimensional RBC function to efficiently estimate and remove vignetting. Log-intensity entropy (LE) [21] is a useful measure for vignetting estimation based on the hypothesis that the vignetting-free images are more likely to have a low entropy, and it is effective to remove vignetting by minimizing the LE measure. The variational-Bayesian (VB) algorithm [22] restores vignetting-free images by minimizing local image variations based upon the observation that the local variations in natural images should be small at most pixels. The non-parametric vignetting correction (NPVC) algorithm [12] uses an iterative sliced histogram routine to estimate vignetting based on the observation that the pixel intensity at different rows and columns of random images would be indicative of potential vignetting artifacts.

These single-image-based approaches are flexible in vignetting correction, but they still face the challenges such as heavy computation, optical center prediction, and vignetting characteristic extraction. Compared with the existing approaches, our algorithm estimates vignetting with the guidance of a novel constant chromaticity prior. Moreover, our algorithm comprehensively considers the issues of computational cost and optical center prediction to improve the generalization ability in practical applications.

III. Our Optical Vignetting Model

Current assembled imaging systems, such as multispectral imaging systems [10], [11] and microscopes [12], contain optical components from different manufacturers designed for specific vision tasks. The difference of apertures may inevitably cause vignetting effect due to the optical occlusion. We propose a specific aperture limit optical model to accurately estimate this type of vignetting. As illustrated in Fig. 1, the imaging components with a small aperture block part of the light entering the lens and cause the vignetting effect. With the increase of incident angle, the corresponding pixel is farther from the optical center and receives less light due to the occlusion. Vignetting correction needs a precise estimation of the attenuation ratio of each pixel, which relates to the intrinsic optical parameters of the imaging system.

Our aperture limit model is constructed based on several main assumptions: 1) the aperture of the imaging components is cylindrical, and consequently, the brightness falloff is radial symmetrical; 2) the targets are far away and thus the incident light is parallel, and 3) the quantum response of the imaging sensor is linear.

Inspired by the light obstruction estimation in the VC model [7] and KW model [8], we use the ratio of the current exit pupil and the maximal exit pupil to model the vignetting function $V(r)$ as

$$V(r) = \frac{S(r)}{S_{\max}}, \tag{7}$$

where $S(r)$ denotes the current exit pupil whose incident angle can be computed according to the distance r between the optical center and the pixel, and $S_{\max}$ denotes the maximal exit pupil with an incident angle of zero. According to the optical analysis of Fig. 1, the current exit pupil $S(r)$ can be formulated as

$$S(r) = 2\left(R^2 \arccos\frac{d(r)}{R} - d(r)\sqrt{R^2 - d^2(r)}\right), \tag{8}$$

where R denotes the radius of the aperture, and $d(r)$ denotes the offset of the exit pupil. $d(r)$ is related to the incident angle α and can be computed as

$$d(r) = \frac{T \cdot \tan\alpha}{2} = \frac{T\eta r}{2f}, \tag{9}$$

where T denotes the thickness of the aperture, f denotes the focal length, and η denotes the size of a pixel. The maximal exit pupil $S_{\max}$ equals the area of the aperture, which is πR^2. Hence, (7) can be rewritten as

$$\begin{aligned} V(r) &= \frac{2}{\pi}\left(\arccos\frac{d(r)}{R} - \frac{d(r)}{R}\sqrt{1 - \left(\frac{d(r)}{R}\right)^2}\right) \\ &= \frac{2}{\pi}\left(\arccos\frac{T\eta}{2fR}r - \frac{T\eta}{2fR}r\sqrt{1 - \left(\frac{T\eta}{2fR}r\right)^2}\right). \end{aligned} \tag{10}$$

Since T, η, f, and R are the intrinsic parameters of an imaging system, we define an occlusion parameter $k = \frac{T\eta}{2fR}$ to simplify (10) to

$$V(r) = \frac{2}{\pi}\left(\arccos kr - kr\sqrt{1 - (kr)^2}\right). \tag{11}$$

As a result, we can effectively remove vignetting by estimating only a single occlusion parameter k instead of all mechanical parameters of the imaging system.

IV. Our Vignetting Correction Algorithm

In this section, we first introduce the constant chromaticity prior derived from the theoretical and image statistical perspectives. Then we propose a vignetting correction algorithm under the guidance of the constant chromaticity prior. Next, we present the details of two main modules for vignetting correction. Finally, we extend our algorithm to other types of vignetting.

A. Constant Chromaticity Prior

It is critical to extract vignetting characteristics in an image although these low-frequency features are mixed with the scene information. Based on the analysis of natural images with vignetting effect, we present a novel *constant chromaticity prior* for vignetting estimation, i.e., the chromaticity of a pixel is barely affected by vignetting although the brightness significantly decreases.

In the following we prove the constant chromaticity prior theoretically. For a given vignetted image $\mathbf{Z}$, its chromaticity image [25] $\widetilde{\mathbf{Z}}$ is computed as

$$\widetilde{\mathbf{Z}}(x, y) = \frac{\mathbf{Z}(x, y)}{\sum_c Z_c(x, y)}, \tag{12}$$

where c denotes the channel index. According to the imaging models [26], the channel image $Z_c(x, y)$ is

$$Z_c(x, y) = \int_\lambda l(\lambda)\rho(\lambda, x, y)t_c(\lambda)s(\lambda)V(x, y)d\lambda, \tag{13}$$

where $l(\lambda)$ denotes the spectral energy distribution of the light source, $\rho(\lambda, x, y)$ denotes the spectral reflectance at pixel (x, y), $t_c(\lambda)$ denotes the spectral transmittance of the c-th filter, $s(\lambda)$ denotes the spectral sensitivity of the sensor, and $V(x, y)$ denotes the intensity attenuation due to vignetting. Based on the existing optical models [7], [8], light obstruction is the main cause of vignetting. The obstruction degree only involves the intrinsic optical parameters and is independent of spectral wavelength. Therefore, (13) can be reformulated as

$$\begin{aligned} Z_c(x, y) &= V(x, y)\int_\lambda l(\lambda)\rho(\lambda, x, y)t_c(\lambda)s(\lambda)d\lambda \\ &= V(x, y)I_c(x, y), \end{aligned} \tag{14}$$

where $I_c(x, y)$ denotes the intensity of the c-th channel image of the vignetting-free image $\mathbf{I}$. By substituting (14) into (12) we have $\widetilde{\mathbf{Z}}(x, y) = \widetilde{\mathbf{I}}(x, y)$, which indicates that $\widetilde{\mathbf{Z}}$ equals the chromaticity image $\widetilde{\mathbf{I}}$ of the vignetting-free image.

We have analyzed a large number of natural images to validate the effectiveness of the constant chromaticity prior. Fig. 2 provides several examples acquired by a multispectral imaging system [10]. It is observed that the chromaticity images are free from vignetting such as the sky and road regions. As the above theoretical analysis does not use a specific type of vignetting, the constant chromaticity prior is generic for most imaging systems.

Under the guidance of the constant chromaticity prior, we can select pixels of the same chromaticity to accurately predict vignetting function. We exploit chromaticity to correct

Fig. 2. Real vignetted images acquired using a three-channel shortwave infrared imaging system [10]. The three-channel infrared images are displayed in pseudo-color space. The vignetting arises from the light obstruction by small apertures in front of the lens. The first row shows the three-channel SWIR images, and the second row shows the corresponding chromaticity images.

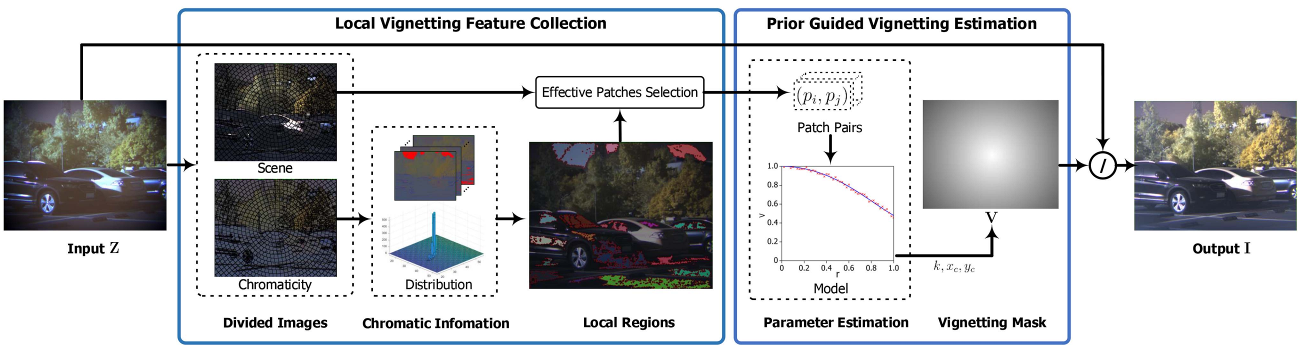

Fig. 3. Framework of our vignetting correction algorithm. In the *local vignetting feature collection* module, we obtain a series of local regions for vignetting estimation according to the analysis of chromatic and spatial information. In the *prior guided vignetting estimation* module, we estimate model parameters using patch pairs guided by constant chromaticity prior, and generate vignetting mask. Finally, we obtain vignetting-free image by pixel-wise division.

vignetting for its two advantages. First, the chromaticity reflects the chromatic "fingerprints" of the objects and can benefit the segmentation of homogeneous regions. Second, the vignetting-invariant chromaticity can help the precise estimation of brightness attenuation. Based on these two advantages, we can effectively extract low-frequency vignetting characteristics from the complex scene information and restore vignetting-free images.

B. Algorithm Framework

Fig. 3 illustrates the framework of our algorithm under the guidance of the constant chromaticity prior. It consists of two main modules to collect vignetting features and estimate vignetting, respectively.

The first module analyzes the chromatic and spatial information of the image, and selects the local regions that are beneficial to vignetting feature extraction. For a given vignetted image $\mathbf{Z}$, we generate its chromaticity image and divide the images into patches for computation efficiency. We cluster patches with the same chromaticity from the spatial dimension. The clustered regions will be applied to collect effective patches for vignetting parameter computation.

The second module estimates the vignetting model parameters and the optical center based on constant chromaticity prior. We form abundant patch pairs for each clustered region and compute the mean intensity ratio of each patch pair. We exploit the ratios to estimate vignetting since the patches belonging to the same local region should have the same intensity according to the constant chromaticity prior. With the predicted parameters, we generate the vignetting mask $\mathbf{V}$.

Finally, as the vignetting mask $\mathbf{V}$ represents the intensity attenuation of all pixels, we simply employ pixel-wise division to restore the vignetting-free image $\mathbf{I}$.

C. Local Vignetting Feature Collection

As vignetting is a type of low-frequency image deterioration, it is hard to extract vignetting features that are mixed with the scene contents. In our work, we select several local homogeneous regions by analyzing chromatic and spatial information. These regions will be used in vignetting estimation since they contain fewer scene contents affecting characteristic extraction.

Computational cost is an important issue in vignetting feature extraction. For efficiency improvement, we employ a common strategy to divide the image into patches and select uniform patches for vignetting feature extraction. Our experiments on 100,000 random natural images of the MSCOCO dataset [27] validate the applicability of this strategy. For each image, we radially divide the image into 7×7 patches and count the number of patches where the intra-patch pixels maintain the same chromaticity. Fig. 4 presents the number distribution of the

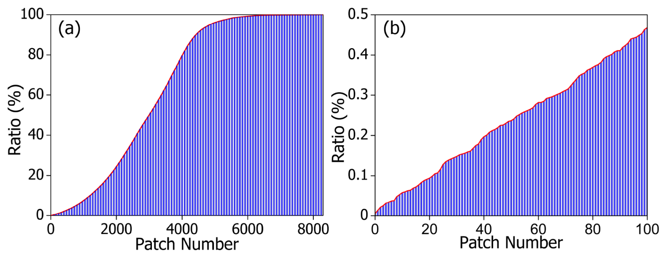

Fig. 4. Statistical distribution of specific 7×7 patches in form of cumulative histograms. For each patch, the inner pixels are of the same chromaticity. (a) The whole cumulative histogram whose patch number is in the range $[0, 8500]$. (b) The partial cumulative histogram whose patch number is in the range $[0, 100]$.

satisfied patches in form of cumulative histograms. According to the aperture limit model, we need at least 4 patches for parameter estimation (occlusion parameter k and optical center (x_c, y_c)), and we find that the correction results are stable and reliable when mare then 40 patches are used. It indicates that more than 99.8% of images satisfy the conditions to predict the parameters. Besides speeding up computation, dividing images into patches can also improve robustness since using the mean intensity of a patch can filter out noise in vignetting estimation.

For a given vignetted image $\mathbf{Z}$, we first compute its chromaticity image $\widetilde{\mathbf{Z}}$ using (12). We then split both $\mathbf{Z}$ and $\widetilde{\mathbf{Z}}$ into 7×7 patches to reduce computational cost. We compute the mean and variance for each chromaticity image patch, and only keep the patches whose chromaticity variances are below the threshold 0.01. Then, we compute the mean intensity and the central location of these patches in the scene image.

For better vignetting estimation, we cluster the selected patches into several homogeneous regions according to chromatic and spatial feature distributions, since vignetting features are more significant in these areas. We obtain the regions through the following two steps.

Step 1: We count the chromaticity distribution of all satisfactory patches. Based on this distribution, we divide the patches into different bins within which the patches are considered to have the same chromaticity. In our work, we empirically set the chromaticity bin interval to $\frac{1}{256}$.

Step 2: We cluster the patches in the spatial dimension. For the patches with the same chromaticity, we apply the popular density-based clustering algorithm DBSCAN [28] to obtain a series of clusters, and regard each cluster as a homogeneous region. In this work, we empirically set the parameters, eps-neighborhood and minimum neighbors, to 28 and 10, respectively.

As a result, we efficiently collect homogeneous regions containing features for further vignetting estimation.

D. Prior Guided Vignetting Estimation

In natural vignetting-free images, the patches in a local region are very likely to have the same intensity, since this region indicates the surface of the same material determined by chromaticity. As vignetting barely affects chromaticity according to the constant chromaticity prior, we can predict the intensity attenuation in a local region by comparing two patches. We exploit the collected regions to jointly estimate the vignetting model parameters and optical center.

In this work, we estimate vignetting by comparing the mean intensity of any two patches within a region. We assume there are N_r regions, and the intensity ratio $\gamma_{i,j}^n$ of two patches in the nth region is

$$\gamma_{i,j}^n = \frac{\bar{Z}_i^n}{\bar{Z}_j^n} = \frac{\bar{I}_i^n \cdot V(r_i)}{\bar{I}_j^n \cdot V(r_j)}, \tag{15}$$

where $\bar{Z}_i^n$ denotes the mean intensity of the i-th patch in the vignetted image $\mathbf{Z}$, $\bar{I}_i^n$ denotes the mean intensity of the ith patch in the vignetting-free image $\mathbf{I}$, and $r_i = \sqrt{(x_i - x_c)^2 + (y_i - y_c)^2}$ denotes the distance between the patch center (x_i, y_i) and the optical center (x_c, y_c). These two patches are supposed to have the same intensity in $\mathbf{I}$ since they belong to the same local region. Then (15) can be rewritten as

$$\gamma_{i,j}^n = \frac{\bar{Z}_i^n}{\bar{Z}_j^n} = \frac{V(r_i)}{V(r_j)}, \tag{16}$$

which shows that the vignetting ratio equals to the intensity ratio of the corresponding patches. With the relationship $V(r_i) = \gamma_{i,j}^n V(r_j)$, we can estimate the vignetting function $V(r)$ and the optical center (x_c, y_c) from a series of equations.

Although the parameter prediction only needs a few patch pairs, the computation can be affected by noise and outliers. Thus, we collect various patch pairs using multiple regions and construct an intra-region loss function for each region. The loss function of the n-th region is formulated as

$$\varepsilon_n = \sum_{i,j \in \text{region}_n} \beta_{i,j}^n (V(r_i) - \gamma_{i,j}^n V(r_j))^2, \tag{17}$$

where $\beta_{i,j}^n$ is a weight function. In modeling the weight, it is important to assign higher weights to those patch pairs with a larger radius ratio, since the significant vignetting variation is more useful for parameter prediction. Consequently, $\beta_{i,j}^n$ is formulated as

$$\beta_{i,j}^n = \max\left\{\frac{r_i}{r_j}, \frac{r_j}{r_i}\right\}. \tag{18}$$

Hence, we solve the vignetting function parameter k and the optical center (x_c, y_c) as follows:

$$k^*, x_c^*, y_c^* = \arg\min_{k, x_c, y_c} \sum_{n=1}^{N_r} \varepsilon_n,$$
$$\text{s.t.} \quad k > 0, \ (x_c, y_c) \in \Phi_c, \tag{19}$$

where Φ_c denotes the center area of the image. We simply constrain k to be non-negative as it is composed of the mechanical parameters of the imaging system. Based on the fact that the optical axes of imaging components are assembled to almost coincide, we also constrain the optical center to locate in the image center neighborhood of which the size is customized according to applications. Moreover, we use the form of sum rather than mean in ε_n to improve the algorithm robustness, since it ensures that the large regions with more features contribute more to the parameter estimation.

To improve robustness, we employ RANSAC [29] to predict the vignetting parameters, with which we compute the intensity attenuation ratio for each pixel and form the mask $\mathbf{V}$ to correct vignetting. Then we obtain the vignetting-free image

$$\mathbf{I} = \mathbf{Z} \oslash \mathbf{V}, \tag{20}$$

where $\oslash$ denotes pixel-wise division.

E. Extension to Other Vignetting Models

Since the constant chromaticity prior is generic, we can extend our algorithm to correct other types of vignetting using different optical models. The main difference between the vignetting models is the number and constraints of the parameters, which means we do not need to adjust the details of the local feature collection. To compute the loss function of the n-th local region with the vignetting model $V(r, \mathbf{k})$, where $\mathbf{k} = [k_1, k_2, \ldots, k_m]$ comprises the m vignetting model parameters, we reformulate (17) as

$$\varepsilon_n = \sum_{i,j \in \text{region}_n} \beta^n_{i,j}(V(r_i, \mathbf{k}) - \gamma^n_{i,j} V(r_j, \mathbf{k}))^2. \tag{21}$$

Consequently, we estimate the model parameters and optical center by reformulating (19) as

$$\begin{aligned} &\mathbf{k}^*, x_c^*, y_c^* = \arg \min_{\mathbf{k}, x_c, y_c} \sum_{n=1}^{N_r} \varepsilon_n, \\ &\text{s.t.} \quad \mathbf{k}_d \preceq \mathbf{k} \preceq \mathbf{k}_u, \ \ (x_c, y_c) \in \Phi_c, \end{aligned} \tag{22}$$

where $\mathbf{k}_d$ and $\mathbf{k}_u$ denote the value range boundary of the parameters. With sufficient patch pairs, we can efficiently solve the model parameters and optical center. Note that $\mathbf{k}_d$, $\mathbf{k}_u$, and $\mathbf{k}$ are scalars respectively when the vignetting model, such as the axis-off model [5] and our aperture limit model, contains only one parameter.

F. Algorithm Summary

To clarify, we summarize our algorithm for vignetting correction in Algorithm 1.

Algorithm 1: Correcting Vignetting Effect in Images.

Input: Vignetted image $\mathbf{Z}$, decomposion template $\mathbf{P}$.
Output: The vignetting-free image $\mathbf{I}$.
Compute the chromaticity image $\widetilde{\mathbf{Z}}$ using (12);
Compute the satisfactory patches using $\mathbf{Z}$, $\widetilde{\mathbf{Z}}$, and $\mathbf{P}$;
Separate patches into C chromaticity categories;
for $n = 1$ **to** C **do**
| Cluster patches based on spatial density;
end
Generate N_r homogeneous regions;
for $n = 1$ **to** N_r **do**
| Compute all intensity ratio using (15);
end
Compute the parameters using (22);
Compute the vignetting mask $\mathbf{V}$;
Compute $\mathbf{I}$ using (20).

V. Experiments

In the following, we first introduce the experimental settings of the synthetic and real datasets. Then we validate our aperture limit model by analyzing vignetted images. Next, we present the correction results on the synthetic images with aperture limit vignetting. We then assess the algorithm on other vignetting models. Finally, we evaluate the correction effectiveness on real-world vignetted images.

To validate the effectiveness of our vignetting correction algorithm, we use synthetic images to assess the restoration quantitatively with respect to ground truth, and exploit the real-world images for qualitative comparison. We employ our aperture limit model and the extended KW model [9] to generate synthetic images. We compare the vignetting correction effectiveness of our algorithm with the state-of-the-art ones including GDS [19], RBC [20], LE [21], VB [22], and NPVC [12].

A. Experimental Settings

We conduct experiments on synthetic and real-world images, and evaluate the performance of our vignetting correction algorithm. We randomly select natural images from the MSCOCO [27] dataset that contains different scenes and complex objects, and generate synthetic images using different vignetting models. The images used in our work consist of the following ones.

1) Synthetic Images With Aperture Limit Vignetting: We use the aperture limit model to generate vignetted images. Considering the resolution difference between images, we normalize the radius r to [0,1] and scale k to $\bar{k} = k \times r_{\max}$. Via the estimation of different imaging systems, $\bar{k}$ may be reasonably sampled in the range $[0.1, 0.9]$. The synthetic images with aperture limit vignetting consist of two parts: a) we use 300 random images to generate 300 vignetted images with 300 random $\bar{k}$ within [0.1,0.9]. These images are used to evaluate the correction effectiveness of different algorithms; b) we select another 60 images to validate the effectiveness of the algorithm under different vignetting level. For each image, we generate 9 vignetted ones by setting $\bar{k}$ from 0.1 to 0.9 with step 0.1. These synthesized images are used to validate the robustness of algorithms.

2) Synthetic Images With Extended KW Vignetting: Since the extended KW model [9] comprises the factors that are common in other vignetting models, we use it to generate vignetted images for the correction performance evaluation on other types of vignetting. In detail, we select 60 natural images and apply 20 different vignetting functions to each image. We generate vignetting functions using (6) with parameter sets of $\{f, \alpha_1, \alpha_2, \alpha_3, \alpha_4\}$ while neglecting the tilt effect, where we set $f = \{250, 500, 1300, 2000, 3000\}$ and randomly set α_i.

3) Real-World Images: We acquire some images with aperture limit vignetting using different imaging systems, including a three-channel shortwave infrared imaging system [10] and a

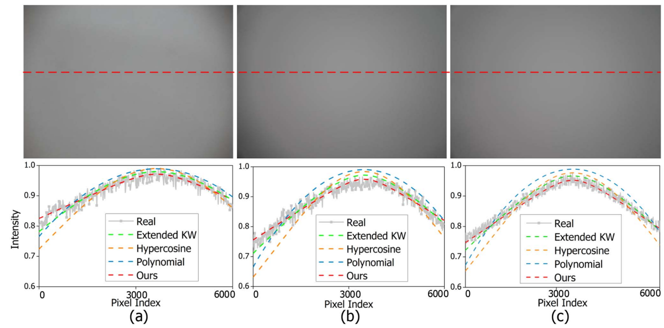

Fig. 5. Three vignetted images acquired with three tubes. The first row shows the images of whiteboard. The second row shows the normalized intensity of the 1600th row (red dashed line) of the vignetted image and fitting curves of different vignetting models. The average pixel intensity errors of Extended KW model [9], Hypercosine model [24], Polynomial model [14], and our model are 0.019, 0.041, 0.036, and 0.012 respectively. (a) $f = 70\,\text{mm}$, $T = 60\,\text{mm}$, and $R = 39\,\text{mm}$. (b) $f = 50\,\text{mm}$, $T = 60\,\text{mm}$, and $R = 35\,\text{mm}$. (c) $f = 50\,\text{mm}$, $T = 50\,\text{mm}$, and $R = 35\,\text{mm}$.

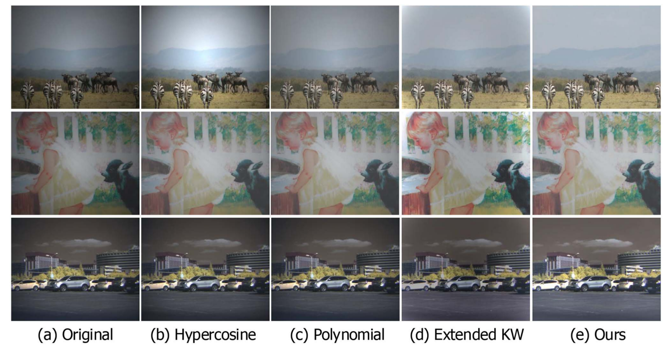

Fig. 6. Corrected images using different vignetting models and our correction algorithm. The first row shows the synthetic image selected from the MSCOCO dataset. The second rows shows the real-world image captured by a visible multispectral imaging system. The third row shows the real-world image captured by a shortwave infrared imaging system. (a) Original images with aperture limit vignetting. (b) Images corrected by the hypercosine model [24]. (c) Images corrected by the polynomial model [14]. (d) Images corrected by the extended KW model [9]. (e) Images corrected by our aperture limit algorithm.

visible multispectral imaging system [11]. We also download a series of real-world images[1] with conventional vignetting which are captured by different cameras with various imaging settings.

Note that the optical centers of vignetting in all synthetic images are randomized in a 30×30 neighborhood of the image center. We employ four different metrics to assess algorithms quantitatively, i.e., peak signal-to-noise ratio (PSNR) [21], structural similarity index measure (SSIM) [21], ΔE_{ab}[30], and color image-difference (CID) [31]. PSNR and SSIM metrics measure global intensity quality, and ΔE_{ab} and CID measure color quality.

B. Validation on Aperture Limit Model

We use reference images, synthetic images, and real-world images to validate the aperture limit model. We compare our model with 6-th order even polynomial model [14], hypercosine model [24], and extended KW model [9] on the images with aperture limit vignetting.

We capture the images of a uniform Labsphere whiteboard using a SONY A6100 camera attached with a specifically designed tube. By exchanging tubes of different thickness and radius we can get a set of vignetted images. For each vignetted image, we compute the occlusion parameter k to predict the brightness attenuation, and also estimate the unknown parameters in other vignetting models using the least square method. Fig. 5 shows three vignetted examples and the fitting curves. The hypercosine model and polynomial model estimate brightness attenuation satisfactorily in the regions around the optical center, but they cannot work at the image edges. Although the extended KW model improves the vignetting estimation according to optical analysis, it may be unsuitable for this kind of vignetting due to different optical factors. In comparison, our aperture limit model fits the vignetting effect well with different imaging parameters, and produces the lowest errors of the whole images.

[1]Data available at https://github.com/GUOYI1/Vignetting_corrector/tree/master/data

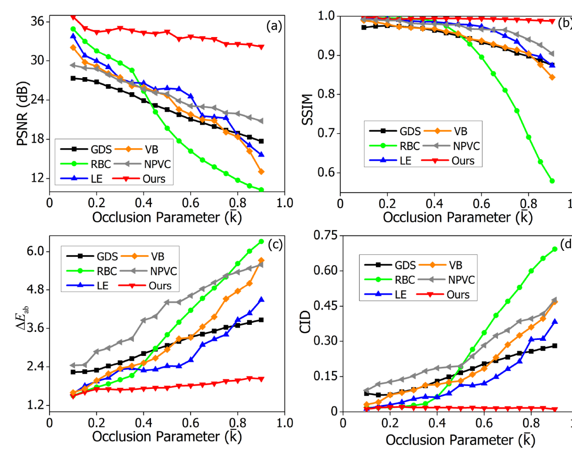

Fig. 7. Evaluation on the corrected images produced by GDS [19], RBC [20], LE [21], VB [22], NPVC [12] and our algorithm. (a) Mean PSNR. (b) Mean SSIM. (c) Mean ΔE_{ab}. (d) Mean CID.

To estimate the performance in image edge, we also select the 10-th and 11-th rows of the vignetted images and compute the average pixel intensity errors of different vignetting models. The results of the Extended KW model [9], Hypercosine model [24], Polynomial model [14] and our model are 0.028, 0.073, 0.064, and 0.014, respectively, which indicates that our model has a better performance of vignetting prediction around edges.

We apply our correction algorithm and different vignetting models on the synthetic and real-world images with aperture limit vignetting. Table I shows the average image quality metrics of 300 synthetic images. It demonstrates that the proposed aperture limit model can produce better image restoration performance thanks to the accurate modeling of brightness attenuation. Fig. 6 illustrates the correction results of the synthetic and real-world images. Results of the hypercosine model and the polynomial model remain vignetting effect in image corners. The extended KW model boosts the restoration performance in corners though it may be over-corrected visibly. Our model

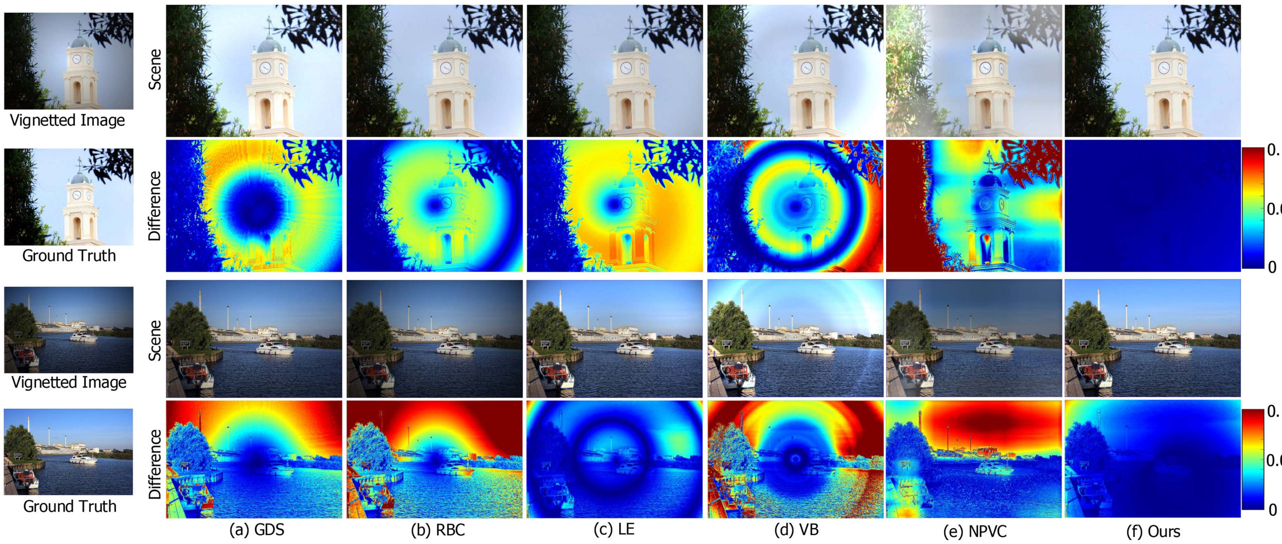

Fig. 8. Image produced by different vignetting correction methods. The vignetted images are generated using aperture limit model. For each scene, the first row illustrates the vignetting corrected images, and the second row shows the scaled difference maps between the corrected images and the corresponding ground truths. (a) Images corrected by GDS [19]. (b) Images corrected by RBC [20]. (c) Images corrected by LE [21]. (d) Images corrected by VB [22]. (e) Images corrected by NPVC [12]. (f) Images corrected by our algorithm.

TABLE I
MEAN PSNR, SSIM, ΔE_{AB}, AND CID OF THE IMAGES CORRECTED USING DIFFERENT VIGNETTING MODELS

Models	PSNR↑	SSIM↑	ΔE_{ab}↓	CID↓
Hypercosine	19.30	0.8804	4.21	0.3570
Polynomial	21.11	0.9165	3.95	0.2252
Extended KW	23.13	0.9640	2.88	0.1297
Aperture limit (ours)	**34.24**	**0.9924**	**1.81**	**0.0118**

TABLE II
MEAN PSNR, SSIM, ΔE_{AB}, AND CID OF THE IMAGES AFTER CORRECTING APERTURE LIMIT VIGNETTING

Methods	GDS	RBC	LE	VB	NPVC	Ours
PSNR↑	22.67	22.45	24.81	23.02	24.25	**34.24**
SSIM↑	0.9408	0.9347	0.9629	0.9486	0.9694	**0.9924**
ΔE_{ab}↓	3.04	3.14	2.75	2.87	3.31	**1.81**
CID↓	0.2805	0.3127	0.3824	0.3573	0.3613	**0.0118**

produces satisfactory results thanks to its suitable optical analysis and modeling.

C. Algorithm Evaluation With Our Aperture Limit Model

Fig. 8 presents the correction results of synthetic images with aperture limit vignetting. It is observed that GDS [19] can accurately estimate vignetting in the center area but it may ignore other parts. RBC [20], LE [21], and VB [22] take into account the restoration effect of the whole image while some vignetting still exist in the form of rings. NPVC [12] can visibly remove vignetting yet it causes new artifacts like haze in the corrected images. In comparison, our algorithm achieves better vignetting correction and the resulting images are closer to ground truths. Table II lists the mean PSNR, SSIM, ΔE_{ab}, and CID of the corrected images, which indicate that our algorithm outperforms other approaches for all metrics.

We evaluate these methods on different levels of aperture limit vignetting, and illustrate the PSNR, SSIM, ΔE_{ab}, and CID curves in Fig. 7. It is observed that the current algorithms deal with light vignetting when $\bar{k} < 0.3$. However, they may work unsatisfactorily as the vignetting becomes thick. In comparison, our algorithm always performs better than the competitors and is more robust to scenarios with different vignetting levels.

TABLE III
MEAN PSNR, SSIM, RMSE, ΔE_{AB}, AND CID OF THE IMAGES AFTER CORRECTING KW VIGNETTING

Methods	GDS	RBC	LE	VB	NPVC	Ours
PSNR	22.71	24.51	24.97	23.86	24.11	**32.23**
SSIM	0.9381	0.9694	0.9757	0.9617	0.9743	**0.9919**
ΔE_{ab}	3.08	2.89	2.71	2.97	2.79	**1.82**
CID	0.1702	0.1344	0.1003	0.1473	0.1874	**0.0215**

D. Algorithm Evaluation With Extended KW Model

We evaluate the vignetting correction algorithms on images with other types of vignetting. To ensure the correction effect, we apply the extended KW model [9] in our algorithm for vignetting estimation. Fig. 9 presents the correction results of some synthetic images. GDS [19] and RBC [20] remove most vignetting but retain a little in the corners. LE [21] and VB [22] improve the image restoration in corners but causes some shadow rings. NPVC [12] removes vignetting effectively but causes color deviation. In comparison, our algorithm produces much better vignetting correction results.

Table III lists the mean PSNR, SSIM, ΔE_{ab}, and CID of the corrected images. It is obvious that our algorithm outperforms

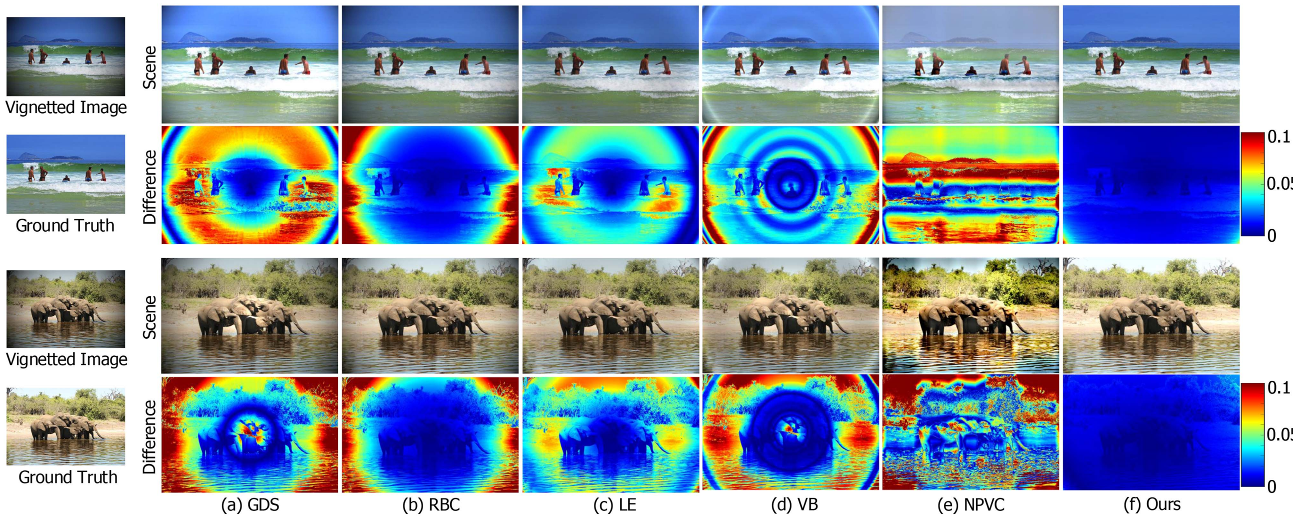

Fig. 9. Image produced by different vignetting correction methods. The vignetted images are generated using the Extended KW model [9]. For each scene, the first row illustrates the vignetting corrected images, and the second row shows the scaled difference maps between the corrected images and the corresponding ground truths. (a) Images corrected by GDS [19]. (b) Images corrected by RBC [20]. (c) Images corrected by LE [21]. (d) Images corrected by VB [22]. (e) Images corrected by NPVC [12]. (f) Images corrected by our algorithm.

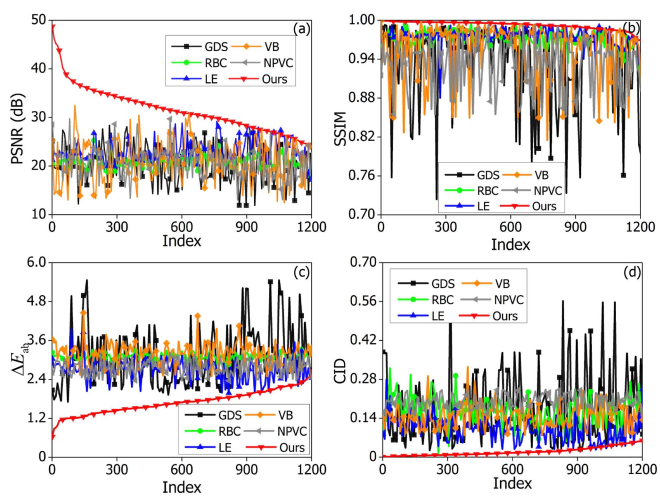

Fig. 10. Evaluation of the total 1200 vignetting correction results produced by GDS [19], RBC [20], LE [21], VB [22], NPVC [12] and our algorithm. (a) PSNR values of the corrected images, sorted in descending order w.r.t. the PSNRs of our algorithm. (b) SSIM values of the corrected images, sorted in ascending order w.r.t. the SSIMs of our algorithm. (c) ΔE_{ab} values of the corrected images, sorted in ascending order w.r.t. the ΔE_{ab} of our algorithm. (d) CID values of the corrected images, sorted in ascending order w.r.t. the CIDs of our algorithm.

the other state-of-the-art methods. Fig. 10 shows the metric curves of the total 1200 vignetting corrected synthetic images. GDS can effectively correct vignetting in some scenes but fails when gradient distributions are difficult to extract. With the assistance of strict constraints in vignetting estimation, RBC, LE, VB, and NPVC can produce results that are more stable. Our algorithm produces best correction results under most circumstances, thanks to the effective extraction of vignetting features.

E. Evaluation on Images With Real Vignetting

We evaluate the vignetting correction methods on real-world vignetted images. When dealing with the images captured by imaging systems with small apertures [10], [11], we employ our aperture limit model for parameter estimation. As shown in Fig. 11, all competitors cannot correct the vignetting around corners. In comparison, our algorithm corrects most vignetting effects in the images.

We use the extended KW model [9] to estimate vignetting in images downloaded online. Fig. 12 illustrates some correction results. It is observed that the images corrected by those state-of-the-art methods still have some vignetting artifacts in the form of dark corners, rings, or grids. Our algorithm corrects most vignetting effects and the resultant images are perceptually more natural.

TABLE IV
MEAN EXECUTION TIME OF PROCESSING AN IMAGE WITH VIGNETTING

Methods	GDS	RBC	LE	VB	NPVC	Ours
Time (s)	0.636	1.043	16.317	7.943	0.971	1.131

F. Running Time

We compare the speed between our algorithm and the state-of-the-art methods on both the synthetic and real-world images including 2200 images of resolutions from 1280×720 to 2048×1080. All algorithms are implemented in Matlab and run on a PC with 2.6 GHz Intel Core i7 CPU and 16 G memory.

Table IV shows the mean execution time of different algorithms. The time cost of GDS is the shortest among all algorithms but its correction performance is relatively worse than others. RBC can efficiently remove vignetting by estimating parameters from a 1-D vector. LE produces better correction results based on the strict constraints which also increases the computational cost. VB estimates vignetting with an iterative strategy to make the result stable and accordingly increases its execution time. NPVC restores images by extracting vignetting features from

Fig. 11. Correction results of some real-world vignetted images captured by a multispectral imaging system. (a) Original images. (b) Images corrected by GDS [19]. (c) Images corrected by RBC [20]. (d) Images corrected by LE [21]. (e) Images corrected by VB [22]. (f) Images corrected by NPVC [12]. (g) Images corrected by our algorithm.

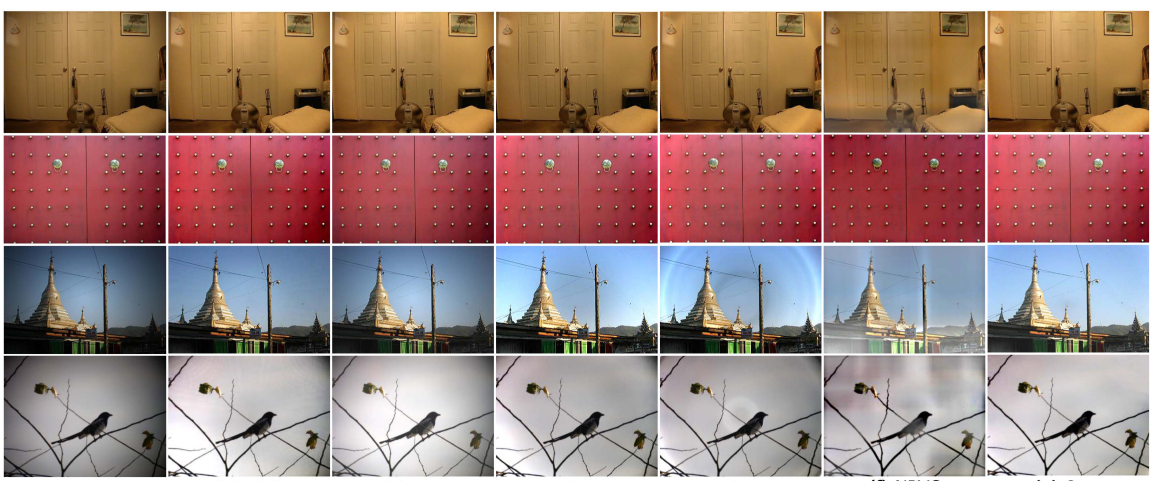

Fig. 12. Correction results of some real-world vignetted images downloaded online. (a) Original images. (b) Images corrected by GDS [19]. (c) Images corrected by RBC [20]. (d) Images corrected by LE [21]. (e) Images corrected by VB [22]. (f) Images corrected by NPVC [12]. (g) Images corrected by our algorithm.

columns and rows whose computation is less than processing a 2-D image. In comparison, our algorithm takes a short execution time since it solves vignetting parameters from the pixel intensity ratio without complex computation. Thanks to the application of RANSAC strategy [29], the efficiency of our algorithm are also less affected by image resolutions. Moreover, our algorithm effectively extracts vignetting features from the whole image and outperforms the existing methods.

VI. Conclusion

We have proposed an algorithm for single-image vignetting correction. For accurate estimation of vignetting caused by light occlusion, we introduce an optical aperture limit model that produces a close fit to vignetting common in current imaging systems. Guided by a novel constant chromaticity prior, our algorithm efficiently extracts vignetting features according to chromatic and spatial information, and solves parameters for vignetting correction. Experimental results have validated the effectiveness of our algorithm on a broad range of images with different vignetting levels.

A limitation of our vignetting correction algorithm is its moderately unsatisfactory restoration in the corners of images since the vignetting is jointly determined by optical center and model parameters that are difficult to estimate. Considering the vignetting is a low-frequency image degradation and the neural network maintains a satisfactory performance on extracting this kind of features, we aim to design a small convolutional neural network to extract the vignetting features in our future work, and apply the proposed constant chromaticity prior to construct a effective loss function for parameter prediction. In addition, we will also plan to improve the computational efficiency of the algorithm for practical applications.

REFERENCES

[1] X. Ye et al., "Superpixel guided network for three-dimensional stereo matching," *IEEE Trans. Comput. Imag.*, vol. 8, pp. 54–68, 2022.

[2] A. Jerez, S. Pinilla, and H. Arguello, "Fast target detection via template matching in compressive phase retrieval," *IEEE Trans. Comput. Imag.*, vol. 6, pp. 934–944, 2020.

[3] F. Zhang, T. Yang, L. Liu, B. Liang, Y. Bai, and J. Li, "Image-only real-time incremental UAV image mosaic for multi-strip flight," *IEEE Trans. Multimedia*, vol. 23, pp. 1410–1425, 2021.

[4] H. Shi, H. Li, Q. Wu, and K. N. Ngan, "Query reconstruction network for referring expression image segmentation," *IEEE Trans. Multimedia*, vol. 23, pp. 995–1007, 2021.

[5] P. Mouroulis, J. Macdonald, and J. Macdonald, *Geometrical Optics and Optical Design*, vol. 39. London, U.K.: Oxford Univ. Press, 1997.

[6] J. Strong, *Concepts of Classical Optics*. North Chelmsford,MA, USA: Courier Corporation, 2012.

[7] N. Asada, A. Amano, and M. Baba, "Photometric calibration of zoom lens systems," in *Proc. Int. Conf. Pattern Recognit.*, 1996, vol. 1, pp. 186–190.

[8] S. B. Kang and R. Weiss, "Can we calibrate a camera using an image of a flat, textureless Lambertian surface?," in *Proc. Eur. Conf. Comput. Vis.*, 2000, pp. 640–653.

[9] Y. Zheng, S. Lin, C. Kambhamettu, J. Yu, and S. B. Kang, "Single-image vignetting correction," *IEEE Trans. Pattern Anal. Mach. Intell.*, vol. 31, no. 12, pp. 2243–2256, Dec. 2009.

[10] B. Yu, Y. Chen, S.-Y. Cao, H.-L. Shen, and J. Li, "Three-channel infrared imaging for object detection in haze," *IEEE Trans. Instrum. Meas.*, vol. 71, 2022, Art. no. 5008513.

[11] S.-J. Chen and H.-L. Shen, "Multispectral image out-of-focus deblurring using interchannel correlation," *IEEE Trans. Image Process.*, vol. 24, no. 11, pp. 4433–4445, Nov. 2015.

[12] B. Y. Rao et al., "Non-parametric vignetting correction for sparse spatial transcriptomics images," in *Proc. Med. Image Comput. Comput. Assist. Intervention*, 2021, pp. 466–475.

[13] H. Cao, X. Gu, M. Zhang, H. Zhang, and X. Chen, "Vignetting correction based on a two-dimensional Gaussian filter with harmony for area array sensors," *IEEE Trans. Comput. Imag.*, vol. 8, pp. 576–584, 2022.

[14] D. B. Goldman, "Vignette and exposure calibration and compensation," *IEEE Trans. Pattern Anal. Mach. Intell.*, vol. 32, no. 12, pp. 2276–2288, Dec. 2010.

[15] S. J. Kim and M. Pollefeys, "Robust radiometric calibration and vignetting correction," *IEEE Trans. Pattern Anal. Mach. Intell.*, vol. 30, no. 4, pp. 562–576, Apr. 2008.

[16] A. Litvinov and Y. Schechner, "Addressing radiometric nonidealities: A unified framework," in *Proc. IEEE Comput. Soc. Conf. Comput. Vis. Pattern Recognit.*, 2005, vol. 2, pp. 52–59.

[17] R. Juang and A. Majumder, "Photometric self-calibration of a projector-camera system," in *Proc. IEEE Conf. Comput. Vis. Pattern Recognit.*, 2007, pp. 1–8.

[18] Y. Zheng, S. Lin, and S. B. Kang, "Single-image vignetting correction," in *Proc. IEEE Comput. Soc. Conf. Comput. Vis. Pattern Recognit.*, 2006, pp. 461–468.

[19] Y. Zheng, S. Lin, S. B. Kang, R. Xiao, J. C. Gee, and C. Kambhamettu, "Single-image vignetting correction from gradient distribution symmetries," *IEEE Trans. Pattern Anal. Mach. Intell.*, vol. 35, no. 6, pp. 1480–1494, Jun. 2013.

[20] H. Cho, H. Lee, and S. Lee, "Radial bright channel prior for single image vignetting correction," in *Proc. Eur. Conf. Comput. Vis.*, 2014, pp. 189–202.

[21] L. Lopez-Fuentes, G. Oliver, and S. Massanet, "Revisiting image vignetting correction by constrained minimization of log-intensity entropy," in *Proc. Adv. Comput. Intell.*, 2015, pp. 450–463.

[22] M. Sonogashira, M. Iiyama, and M. Minoh, "Variational-Bayesian single-image devignetting," *IEICE Trans. Inf. Syst.*, vol. 101, no. 9, pp. 2368–2380, 2018.

[23] A. A. Sawchuk, "Real-time correction of intensity nonlinearities in imaging systems," *IEEE Trans. Comput.*, vol. C-26, no. 1, pp. 34–39, Jan. 1977.

[24] W. Yu, "Practical anti-vignetting methods for digital cameras," *IEEE Trans. Consum. Electron.*, vol. 50, no. 4, pp. 975–983, Nov. 2004.

[25] W. Ren, J. Tian, and Y. Tang, "Specular reflection separation with color-lines constraint," *IEEE Trans. Image Process.*, vol. 26, no. 5, pp. 2327–2337, May 2017.

[26] H. Hideaki et al., "System design for accurately estimating the spectral reflectance of art paintings," *Appl. Opt.*, vol. 39, no. 35, pp. 6621–6632, 2000.

[27] T.-Y. Lin et al., "Microsoft COCO: Common objects in context," in *Proc. Eur. Conf. Comput. Vis.*, 2014, pp. 740–755.

[28] M. Ester, H.-P. Kriegel, J. Sander, and X. Xu, "A density-based algorithm for discovering clusters in large spatial databases with noise," in *Proc. Int. Conf. Knowl. Discov. Data Mining*, 1996, pp. 226–231.

[29] M. A. Fischler and R. C. Bolles, "Random sample consensus: A paradigm for model fitting with applications to image analysis and automated cartography," *Commun. ACM*, vol. 24, no. 6, pp. 381–395, 1981.

[30] M. E. Sayed, F. Sammani, and M. A. M. Albashier, "An accurate method to calculate the color difference in a single image," in *Proc. Int. Conf. Robot., Automat. Sci.*, 2017, pp. 1–3.

[31] I. Lissner, J. Preiss, P. Urban, M. S. Lichtenauer, and P. Zolliker, "Image-difference prediction: From grayscale to color," *IEEE Trans. Image Process.*, vol. 22, no. 2, pp. 435–446, Feb. 2013.

Beinan Yu received the B.E. degree from Zhejiang University, Hangzhou, China, in 2019. He is currently working toward the Ph.D. degree with the College of Information Science and Electronic Engineering, Zhejiang University. His research interests include multispectral/hyperspectral imaging and image processing.

Jiacheng Ying received the B.Eng. degree in information engineering in 2020 from Zhejiang University, Hangzhou, China, where he is currently working toward the Ph.D. degree with the College of Information Science and Electronic Engineering. His research interests include multispectral imaging and image processing.

Lun Luo (Member, IEEE) received the B.E. degree from Zhejiang University, Hangzhou, China, in 2018. He is currently working toward the Ph.D. degree with the College of Information Science and Electronic Engineering, Zhejiang University. His research interests include SLAM and LiDAR-based localization.

Si-Yuan Cao received the B.E. degree in electronic information engineering from Tianjin University, Tianjin, China, in 2016, and the Ph.D. degree in electronic science and technology from Zhejiang University, Hangzhou, China, in 2022. He is currently an Assistant Researcher with Ningbo Innovation Center, Zhejiang University. His research interests incldue multispectral/multimodal image registration, homography estimation, place recognition and image processing.

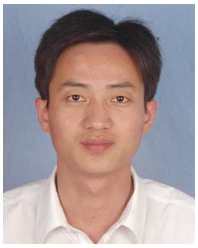

Xiansong Bao received the M.E. degrees in computer technology from the Heifei University of Technology, Hefei, China, in 2018. He is currently a Senior Engineer with Anhui NARI Jiyuan Electric Power System Tech Company Ltd., China. His research interests include device status monitoring and defect detection.

Hui-Liang Shen (Member, IEEE) received the B.E. and Ph.D. degrees in electronic engineering from Zhejiang University, Hangzhou, China, in 1996 and 2002, respectively. He was a Research Associate and Research Fellow with The Hong Kong Polytechnic University, Hong Kong, from 2001 to 2005. He is currently a Full Professor with the College of Information Science and Electronic Engineering, Zhejiang University. His research interests include multispectral imaging, image processing, computer vision, and machine learning.